Applied Catalysis B: Environmental 163 (2015) 288–297

Contents lists available at ScienceDirect

Applied Catalysis B: Environmental

journal homepage: www.elsevier.com/locate/apcatb

Facile in-suit synthesis of $Ag/AgVO_3$ one-dimensional hybrid nanoribbons with enhanced performance of plasmonic visible-light photocatalysis

Wei Zhao, Yang Guo, Yasir Faiz, Wen-Ting Yuan, Cheng Sun*, Shao-Mang Wang, Yue-Hua Deng, Yuan Zhuang, Yong Li, Xiao-Meng Wang, Huan He, Shao-Gui Yang**

State Key Laboratory of Pollution Control and Resource Reuse, School of the Environment, Nanjing University, Nanjing 210023, PR China

ARTICLE INFO

Article history:
Received 7 May 2014
Received in revised form 28 July 2014
Accepted 9 August 2014
Available online 17 August 2014

Keywords:
Plasmonic photocatalysts
Surface plasmon resonance
Photocatalytic activities

ABSTRACT

The novel one-dimension $Ag/AgVO_3$ plasmonic photocatalysts were synthesized via in situ reduction of $AgVO_3$ by $NaBH_4$ at room temperature. The morphologies, optical properties and electronic structures of the synthesized $Ag/AgVO_3$ plasmonic photocatalysts were systematically characterized using a combination of theoretical calculations and experimental techniques. The photocatalytic activities of $Ag/AgVO_3$ photocatalysts were evaluated using photocatalytic degradation of basic fuchsin (BF) dye. The results showed that the photocatalytic efficiency of $Ag/AgVO_3$ was better than that of $AgVO_3$. $Ag/AgVO_3$ demonstrated a high photocatalytic activity with 93.6% of BF decomposed within 90 min. Such enhanced photocatalytic performance could be attributed to the relatively high conductivity and electron-storing capacity of Ag nanoparticles coated on $AgVO_3$ surfaces. These Ag nanoparticles facilitate charge transfer between $AgVO_3$ and Ag nanoparticles, and induce the localized surface plasmon resonance (SPR) that increases electric field and absorption of visible light. The results of the FDTD simulation confirmed that the SPR and the electric field enhancement were caused by the Ag nanoparticles. The theoretical calculation based on DFT indicates that Ag formed could narrow the bandgap of $AgVO_3$ due to the fact that the Ag 5s orbital by association with Ag nanoparticles moves down the CB after hybridization. Meanwhile, the hybridization of O 2p and Ag 4d orbits of $Ag/AgVO_3$ is weak, which is beneficial for valence band electrons to excite into the conduction band. The combined experimental results and characterizations of $Ag/AgVO_3$ suggest that h^+ and $^{\bullet}O_2^-$ are the main reactive species for degradation of BF in the visible light-catalyzed oxidation.

1. Introduction

During the past decades, semiconductor-based photocatalysts have been widely studied for applications in energy conversion and environmental protection [1–5]. TiO_2 has been the most widely used photocatalyst [6] due to its optical and electronic properties, low cost, low toxicity and relatively high chemical stability. However, the relatively wide band gap (3.2 eV) of TiO_2 limits its photocatalytic applications because it only responds to UV irradiation that is only 4% of solar energy. Therefore, great efforts have been devoted to develop the new photocatalysts within the range of visible-light irradiation [7–9]. Two methods are commonly used to exploit visible-light photocatalysts. One is to generate intermediate energy levels between the conduction band (CB) and valence band (VB) by doping metallicor nonmetallic elements to increase the visible light absorbance [10–13]. However, this approach is not that effective because the dopant atoms may serve as sites for charge recombination to decrease photocatalytic performance. An alternative strategy is to develop new materials to effectively utilize visible light, which accounts for about 43% of the incoming solar energy. Since Zou et al. [14] reported direct splitting of water under visible light irradiation with new types of oxide semiconductor photocatalyst, numerous new visible-light-driven catalysts have been studied extensively [15,16].

Silver vanadium oxide (SVO) nanomaterials such as $AgVO_3$, $Ag_2V_4O_{11}$, Ag_3VO_4 and $Ag_4V_2O_7$ have attracted extensive attention owing to their potential applications in rechargeable high-energy density lithium batteries [17] and sensors [18]. The unique hybridization of valence bands of V 3d, O 2p, and Ag 4d orbits in

* Corresponding author. Tel.: +86 89680258.
** Corresponding author.
E-mail addresses: envidean@nju.edu.cn (C. Sun), yangsg@nju.edu.cn (S.-G. Yang).

http://dx.doi.org/10.1016/j.apcatb.2014.08.015
0926-3373/

SVOs manifest a narrow band gap and highly dispersed valence bands, which could be utilized as visible-light-sensitive photocatalyst [19–23]. A typical SVO, β-$AgVO_3$, demonstrates a narrow band gap fit for visible light. Hence it has high a potential be an effective photocatalyst. However, the photocatalytic activity of β-$AgVO_3$ is still insignificant because of its low capability to separate electro-hole pairs, which significantly limits its practical extensive application. Thus, further study is necessary to enhance its photocatalytic performance for the practical application.

An effective way to enhance the photocatalytic activity of photocatalyst is to construct specific nanostructured architectures with various dimensions, including zero-, one-, two-, and three-dimensional (0-D, 1-D, 2-D, and 3-D) nanomaterials, owing to their unique size- and/or shape-dependent physicochemical properties. Recently, considerable efforts have been made to construct $AgVO_3$ of different morphologies. For instance, Chen et al. [24] have prepared β-$AgVO_3$ nanowires with the lengths of several tens of micrometers, which exhibited have much higher charge capacity than that of α-$AgVO_3$ microrods, $Ag_2V_4O_{11}$ nanowires, and commercial $Ag_2V_4O_{11}$ bulk. Bao et al. [25] reported a novel channel structured β-$AgVO_3$ with shallow channels of less than 100 nm in width on the surface. The novel channel-structured β-$AgVO_3$ may have unique applications in microelectrodes or microsensors. Yu and co-workers [26] developed a simple approach for synthesis of β-$AgVO_3$ nanoribbons with widths of 300–600 nm, thicknesses of ca. 40 nm, and lengths of 200–300 μm. Among these SVOs with different morphologies, it is anticipated that one-dimensional (1-D) nanostructures may have excellent photocatalytic performances because the larger aspect ratios and more efficient charge separations on the 1-D nanostructure surfaces will promote the photocatalytic activities [27].

The photocatalytic activities of photocatalysts are significantly improved when the photogenerated holes and electrons could be efficiently separated [28–31]. Surface modification such as Ag nanoparticles on surfaces could enhance the separation rate of photogenerated holes and electrons [32,33] because Ag nanoparticles have the excellent conductivity and strong electron trapping ability. Moreover, the nanostructures of the modified Ag, which can induce localized surface plasmon resonance (SPR) [34–38]. The formation of SPR can not only absorb visible light and convert it to the formation of free energetic electrons, but also promote the electron–hole pair formation rate driven by the electromagnetic field formed nearby the semiconductor [39–44]. Huang has developed a series of Ag@AgX (X = Cl, Br, I) plasmonic photocatalysts, which are highly efficient and stable under visible-light illumination [45–47]. Lin et al. have reported that the Ag@$Ag_3(PO_4)_{1-x}$–ZnO hybrid nanoelectrodes exhibit the strong photooxidative capabilities which may be attributed to the enhanced near-field amplitudes resulting from localized surface plasmon resonance (LSPR) of Ag–core [48]. More importantly, the high stable performance of SVO could be obtained because the Ag particles have already been formed and can act as photogenerated electron traps by accepting electrons from the irradiated SVO [49].

It is hypothesized that the highly efficient photocatalytic performance could be achieved on the catalysts with one dimensional structures and modification of silver nanoparticles for surface plasmon resonance. To test this hypothesis, one dimensional β-$AgVO_3$ nanoribbon was synthesized via in-situ hydrothermal approach; the modification of Ag nanoparticles on surfaces was obtained by reduction of Ag^+ on $AgVO_3$ surfaces by $NaBH_4$. The in-situ growth of Ag on $AgVO_3$ nanoribbon is an important approach to achieve the robust bonding between Ag and $AgVO_3$ nanoribbon, which is essential for the effective charge transfer and separation during photocatalysis. To the best of our knowledge, this novel synthesis of the Ag/$AgVO_3$ plasmonic photocatalyst has not been reported. Ag nanoparticles formed on photocatalyst surfaces were synthesized usually by photoreduction [50,51] which is a complicated and time-consuming method due to the additional photoreduction devices such as xenon lamp and longer reaction time. Herein, the present synthesis method is facile and time saving. This simple synthetic route, which involves no additional photoreduction device, will offer great opportunities for the scale-up in suit preparation of other Ag-loaded Ag-based composite materials.

2. Experimental

2.1. Sample preparation

$AgVO_3$ nanoribbon was synthesized using a hydrothermal process. Specifically, $AgNO_3$ (1.25 mmol) and NH_4VO_3 (1.25 mmol) were mixed in 60 mL of deionized water in ultrasonication for 30 min, then transferred into a Teflon-lined stainless steel autoclave at 180 °C for 24 h. The mixture was allowed to cool down to room temperature, filtrated using filter paper. The solid fractions were washed with deionized water (100 mL) four times and absolute ethanol (50 mL) four times, and then dried under vacuum at 80 °C.

The Ag/$AgVO_3$ plasmonic photocatalyst was prepared via in situ reductive reaction of Ag^+ by $NaBH_4$ at room temperature. $AgVO_3$ (0.25 mmol) was added into 25 mL of aqueous solution to which 25.0 mL of 0.1 mmol/L $NaBH_4$ was added dropwise under vigorous stirring. The suspension turned into blackish brown after 10 min, indicating Ag nanoparticles were formed on the surfaces of $AgVO_3$. The Ag/$AgVO_3$ was obtained by centrifugation at 6000 revolutions per minute for 20 min. Briefly, the sample was denoted as 0.01-Ag/$AgVO_3$. The number of 0.01 represents the molar ration of $NaBH_4$ to $AgVO_3$. Similarly, 0.05-Ag/$AgVO_3$ and 0.10-Ag/$AgVO_3$ were also synthesized by the above procedure except 0.5 and 1.0 mmol/L of $NaBH_4$ solution being added, respectively. The synthesis process is illustrated in Scheme 1.

2.2. Characterization and calculation

X-ray diffraction (XRD) of the samples was performed using an X'PertPRO MPD X-ray diffractometer. X-ray photo-electron spectroscopy (XPS) was used to identify the surface chemical composition and chemical states of the catalysts on a PHI5000 Versa Probe electron spectrometer (ULVAC-PHI, Japan). The field emission scanning electron microscopy (FESEM) images of the catalysts were collected using a FEI-quanta 200F scanning electron microscope with an acceleration voltage of 20 kV. Transmission electron micrographs of Ag/$AgVO_3$ were collected using a FEI-Tecnai F20 (200 kV) transmission electron microscope (TEM). Fluorescence emission spectra were recorded using a FluoroMax 4 type fluorescence spectrophotometer with an excitation wavelength at 350 nm. UV–vis absorption spectra were performed using a Lambda 750 (Perkin Elmer) spectrophotometer at a wavelength range of 200–800 nm. Raman spectra were recorded with a Labram-HR confocal laser Micro-Raman spectrometer equipped with an argon ion laser.

Density functional (DFT) calculations were performed using the plane-wave pseudopotential method as implemented in the CASTEP code [52]. Three-dimensional periodic boundary conditions were used to approximate an infinite solid. The generalized gradient approximation (GGA) in the Perdew–Burke–Ernzerh (PBE) functional form was applied along with the ultrasoft pseudopotentials. Three dimensional finite difference time domain (FDTD) simulations were performed to the model near field distribution of Ag/$AgVO_3$. In the simulations, we assumed that the Ag nanoparticles were uniformly distributed on the *x*–*y* plane of the cross section of $AgVO_3$ nanoribbon and embedded in a background medium of

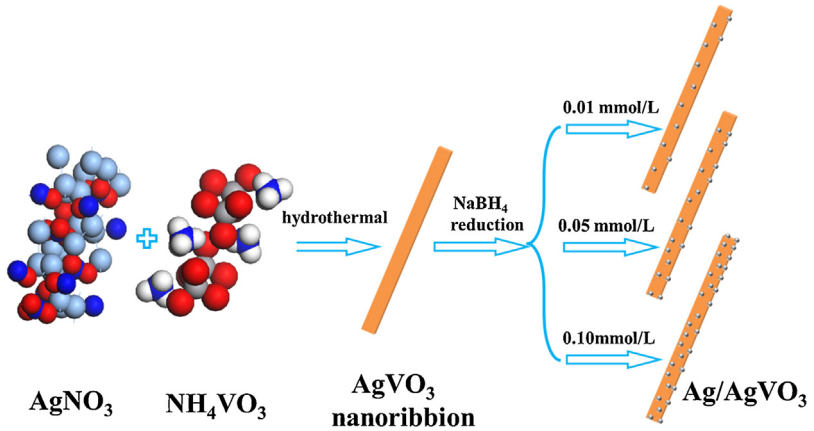

Scheme 1. Schematic illustration of the synthesis of $Ag/AgVO_3$ nanoribbons.

water. Illumination of the $Ag/AgVO_3$ was simulated with a linearly polarized plane wave, propagating in the +Y direction.

2.3. Photocatalytic experiments

Photocatalytic activities of the synthesized photocatalysts were evaluated by reacting with basic fuchsin (BF), malachite green (MG) and crystal violet (CV) under visible light irradiation in a photoreaction apparatus. The visible light was generated from a 500 W Xe lamp irradiation with a 420 nm cut-off filter. The photodegradation of dyes was performed by adding 0.05 g of photocatalyst in 50.0 mL of 20 mg/L dye solution. Prior to irradiation, the suspensions were mixed for 1.0 h in the dark using magnetic stirrers in order to approach adsorption–desorption equilibrium. At given time intervals after initiation of visible light irradiation, 3 mL of samples were collected into centrifuge tubes, centrifuged at 8000 rpm for 10 min and passed through 0.22-μm Millipore membrane. The filtrate was subsequently analyzed by Lambda 750 UV–vis spectroscopy (Perkin Elmer) at the maximum absorption wavelength for each dye. The experiments were conducted in duplicate in separated reactors.

2.4. Detection of reactive species

The detection of the reactive species is similar to the process used for the photodegradation experiment, as described in Section 2.3. Various scavengers were introduced into the BF solution before the addition of the photocatalyst. Benzoquinone (BQ), ammonium oxalate (AO) and isopropanol (IPA) are the scavengers of $^{\bullet}O_2^-$, h^+ and $^{\bullet}OH$, respectively [53,54].

3. Results and discussion

3.1. Structure and morphology

The XRD patterns of the prepared $Ag/AgVO_3$ are shown in Fig. 1 along with pure phase of β-$AgVO_3$ monoclinic structure [JCPDS: 29-11541] for comparison. The (5 0 1) peak is the strongest one, indicating the possible preferential orientation of the $AgVO_3$ nanoribbon [55]. The XRD patterns of the prepared $Ag/AgVO_3$ nanoribbons indicate that the samples are well crystallized and the crystal phase of $AgVO_3$ does not change with forming Ag nanoparticles on $AgVO_3$ surface. The peak at angle 38° clearly demonstrates the formation of face-centered cubic Ag (1 1 1) phase [JCPDS card 04-0783]. The peak intensity of the Ag (1 1 1) phase increased for the $Ag/AgVO_3$ with increasing concentration of $NaBH_4$ used in the synthesis (Fig. 1b–d), indicating the formation of more individual metallic Ag phase on $AgVO_3$ surfaces. Thus, the hybrid nanoribbons have two phase compositions: Ag and $AgVO_3$.

To identify the oxidation states of Ag species in the samples, X-ray photoelectron spectroscopy (XPS) of the 0.05-$Ag/AgVO_3$ was measured (Fig. 2). The spectra revealed that the elements on the surfaces are composed primarily of C (285.0 eV), Ag (368.3 eV and 374.3 eV), V (517.2 and 525.1 eV) and O (532.0 eV). The high-resolution scanning XPS spectra of Ag 3d contained two peaks at approximately 368.3 eV and 374.3 eV which are assigned to the binding energies of Ag $3d_{5/2}$ and Ag $3d_{3/2}$. These two peaks could be further divided into four bands, 368.1 and 374.1 eV for Ag^+ $3d_{5/2}$ and $3d_{3/2}$, and 368.6 and 374.7eV for Ag^0 $3d_{5/2}$ and $3d_{3/2}$. This is consistent with a previous study reported by Zhu et al. [56]. Fig. 2c shows two peaks at 517.2 and 525.1 eV which are attributed to V $2p_{5/2}$ and V $2p_{3/2}$ of V^{5+} in the $AgVO_3$. In addition, the surface Ag^0 content (mole ratio of Ag^0 to Ag^0 and Ag^+) was semiquantitatively estimated by the XPS Ag 3d peak area analysis and summarized in Table 1. It is clear that the content of Ag^0 on the sample surface increased with increasing concentration of $NaBH_4$.

The morphologies of the synthesized $AgVO_3$ are shown in Fig. 3a and b. The relatively low-magnification FESEM image (Fig. 3a) shows an overall view of $AgVO_3$ nanoribbons with thickness of 50–100 nm and width of 100–500 nm. The high-magnification image (Fig. 3b) clearly shows the individual nanoribbon has a smooth surface with the width of ~400 nm. The EDS analysis (Fig. 3c) reveals that the atomic ratio of Ag:V:O is approximately 1:1:3 confirming the composition of $AgVO_3$. The FESEM images of

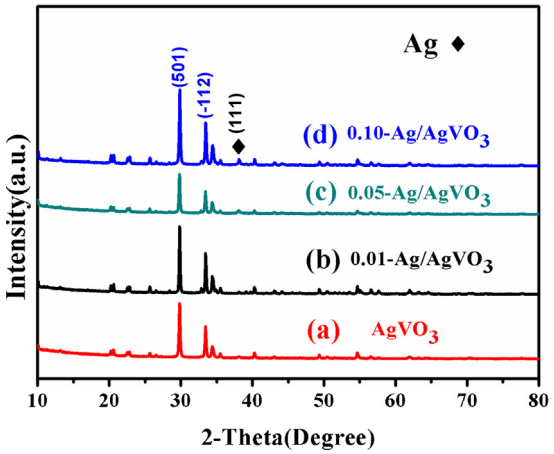

Fig. 1. XRD patterns of the as-prepared samples (♦ mark shows the presence of Ag nanoparticles).

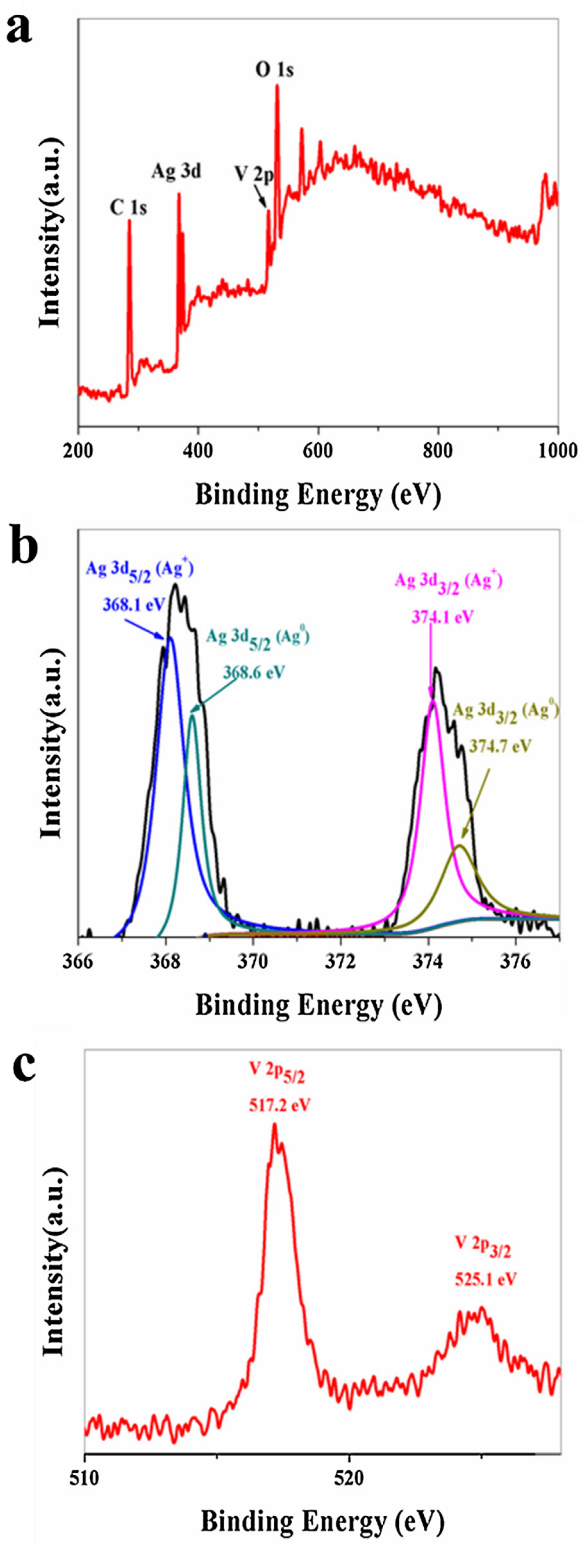

Fig. 2. XPS spectra of (a) the survey, (b) Ag 3d, and (c) V 2p.

the $NaBH_4$-reduced $AgVO_3$ are shown in Fig. 3d–f. The increase of $NaBH_4$ in the reduction resulted in the formation of more Ag nanoparticles on $AgVO_3$ surfaces. The detailed morphologies and microstructures of the 0.05-$Ag/AgVO_3$ nanoribbon are shown in Fig. 4a and b. The width of the nanoribbon was measured at about 400 nm, which is consistent with the FESEM result. The high resolution transmission electron microscopy (HRTEM) showed the

Table 1
XPS Ag 3d peak area analysis of $Ag/AgVO_3$.

Photocatalyst	Peak position (eV)	Peak area	Peak attribution	Surface Ag^0 content
0.01-$Ag/AgVO_3$	367.700	818.410	Ag^+	0.167
	368.300	280.543	Ag^0	
	373.980	578.679	Ag^+	
0.05-$Ag/AgVO_3$	368.100	2061.310	Ag^+	0.329
	368.600	964.642	Ag^0	
	374.100	1288.442	Ag^+	
	374.700	647.370	Ag^0	
0.10-$Ag/AgVO_3$	368.100	188.637	Ag^+	0.934
	368.600	3757.719	Ag^0	
	374.100	215.797	Ag^+	
	374.700	2412.002	Ag^0	

interplanar distances were 0.238 nm for the (1 1 1) crystal plane of Ag and 0.306 nm for the (5 0 1) crystal plane of $AgVO_3$ [57,58]. These results further confirm the formation of Ag nanoparticles located on the $AgVO_3$ surfaces.

3.2. Optical properties

In order to investigate the alterations of optical properties induced by the formed Ag nanoparticles, the $Ag/AgVO_3$ plasmonic photocatalysts were subject to analysis of fluorescence emission spectra, UV–vis absorption spectra and Raman spectra.

The fluorescence emission spectra of the samples are shown in Fig. 5. For the $AgVO_3$, there is one peak at about 580 nm, which is ascribed to the radiative recombination process of self-trapped excitation. The emission spectrum of $AgVO_3$ has relatively high intensity, indicating that electrons and holes of $AgVO_3$ are easy to recombine. The relative intensity of 0.05-$Ag/AgVO_3$ is lower than that of $AgVO_3$, implying that the Ag nanoparticles formed on the surface of the $AgVO_3$ nanoribbon are helpful to suppress the recombination of electrons and holes, which is attributed to the efficient charge transfer between Ag and $AgVO_3$.

UV–vis absorption spectra of $AgVO_3$ and $Ag/AgVO_3$ demonstrate that both $AgVO_3$ and $Ag/AgVO_3$ exhibit strong absorption from ultraviolet light to visible light region. Compared with $AgVO_3$, $Ag/AgVO_3$ samples generally exhibited broad and strong absorption in the visible region, which could be attributed to the surface plasmon resonance (SPR) effect of the Ag nanoparticles on the surfaces of $AgVO_3$ nanoribbons. Obviously, the Ag nanoparticles remarkably enhanced the absorption of light, which potentially increases the formation rate of electron–hole pairs at the Ag and $AgVO_3$ interfaces resulting in improved photocatalytic performance. Significantly, the 0.05-$Ag/AgVO_3$ plasmonic photocatalyst exhibited the highest absorption compared to other $Ag/AgVO_3$ samples. Further increase of Ag content in 0.10-$Ag/AgVO_3$ did not enhance the absorption, which could be attributed to the relatively larger Ag^0 content could cover up the surface of $AgVO_3$, hence reducing the absorption of light [59]. In addition, the band gap energy (E_g) of $AgVO_3$ could be calculated by: $(\alpha h\nu)^n = A(h\nu - E_g)$, where α, h, ν, E_g, and A are the absorption coefficient, Planck's constant, light frequency, band gap and a constant, respectively. The index n depends on the electronic transition of the semiconductor, $n = 2$ for direct-gap semiconductor and $n = 0.5$ for indirect-gap semiconductor. For $AgVO_3$, n is 0.5. The band gap energy of the $AgVO_3$ can be estimated from the intercept of the tangent to the plot of $(Ah\nu)^{1/2}$ vs energy ($h\nu$), and founded to be about 2.0 eV, which is consistent with previous report [60]. The color appearances of the samples are shown on the right of Fig. 6, where the samples from bottom to top are $AgVO_3$, 0.01-$Ag/AgVO_3$, 0.05-$Ag/AgVO_3$ and 0.10-$Ag/AgVO_3$.

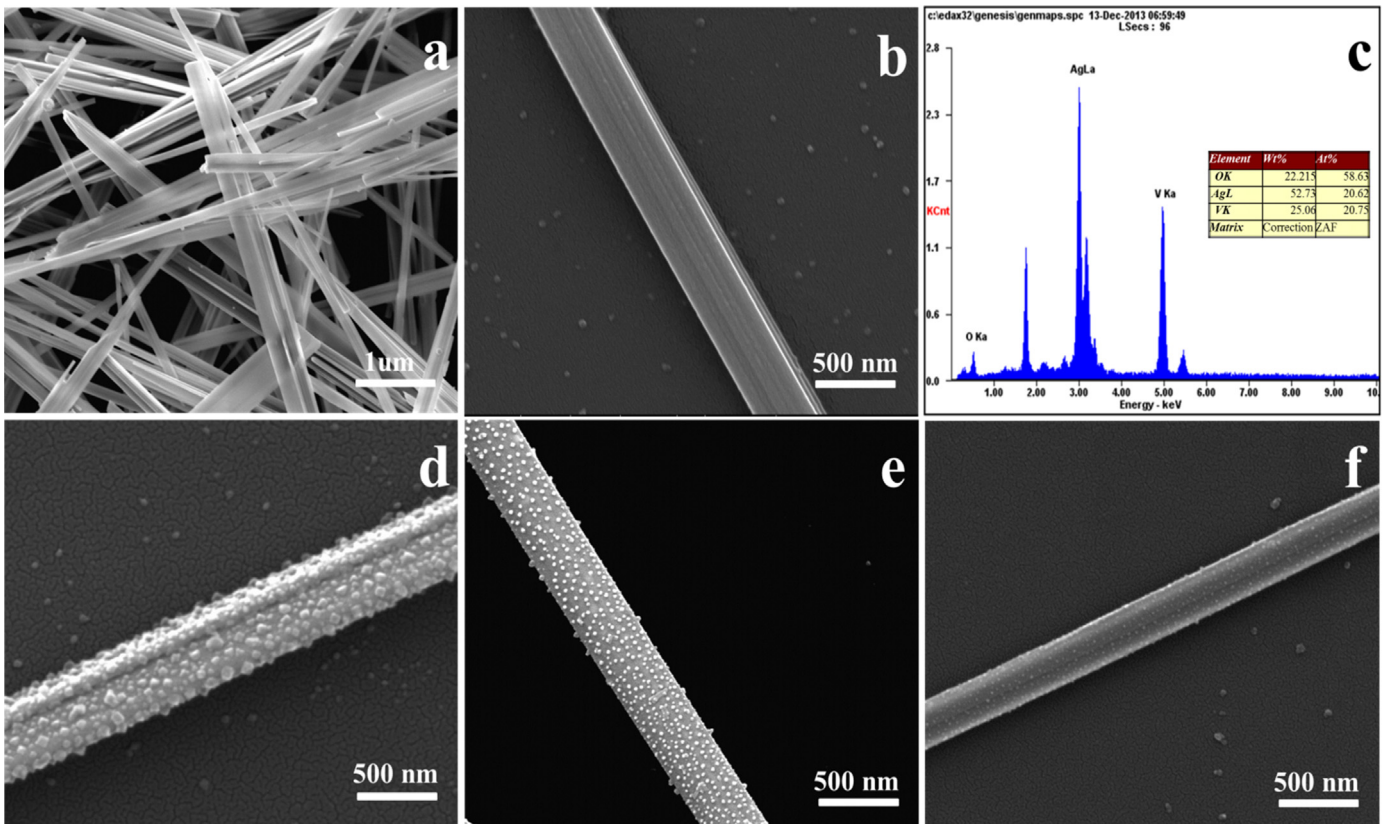

Fig. 3. (a) Low magnification FESEM image of $AgVO_3$, (b) high magnification FESEM image of $AgVO_3$, and (c) EDS pattern of $AgVO_3$. (d–f) The FESEM images of the $Ag/AgVO_3$ synthesized with different $NaBH_4$ concentrations.

Fig. 7 demonstrates Raman spectra of the $AgVO_3$ and 0.05-$Ag/AgVO_3$ nanoribbons. The strong band at 886 cm^{-1} is assigned to either bridging O—V—O or V—O—Ag vibrations. The band at 808 cm^{-1} results from the stretching vibrations of Ag—O—Ag bridges. The bridging V—O—V asymmetric stretching bonds in the polymeric metavanadate chains are reflected at 733 cm^{-1} band. The bands at 386 and 335 cm^{-1} are due to symmetric and asymmetric deformation modes of the VO_4^{3-} tetrahedron. These bands, along with those located at 251, 168, 91, and 70 cm^{-1}, are the clear signature of the $AgVO_3$ nanoribbons [26]. In general, $Ag/AgVO_3$ nanoribbon manifested higher band intensities than those of $AgVO_3$ nanoribbon, which could be due to the effects of surface-enhanced Raman scattering [61–63]. Such enhanced Raman scattering could be related to SPR field induced by Ag nanoparticles on $Ag/AgVO_3$ nanoribbon surfaces.

3.3. *Finite-difference time-domain simulations and density functional calculations*

To explore the SPR and the electric field enhancement caused by the Ag nanoparticles, we simulated the electric field distribution using a three dimensional finite difference time domain

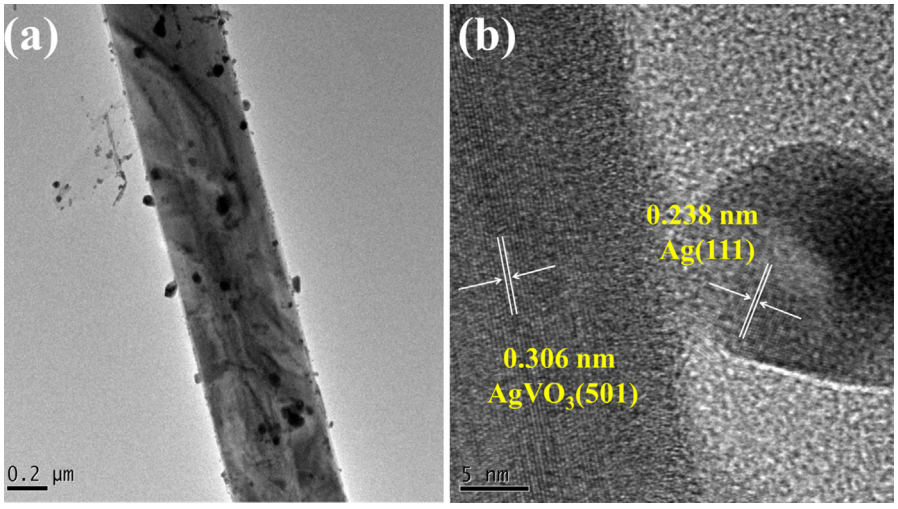

Fig. 4. (a) TEM image of $Ag/AgVO_3$ and (b) HRTEM image of $Ag/AgVO_3$.

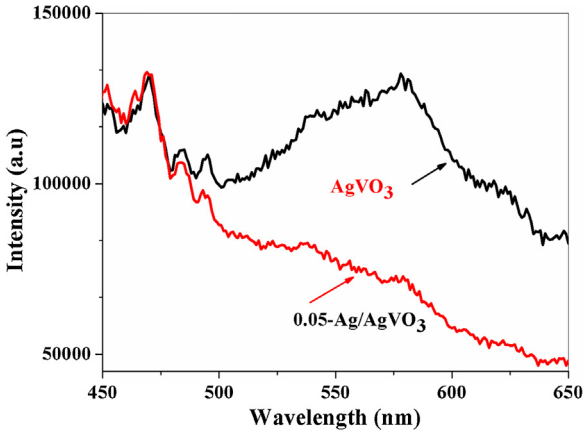

Fig. 5. Room-temperature fluorescence emission spectra of as-prepared $AgVO_3$ and $Ag/AgVO_3$.

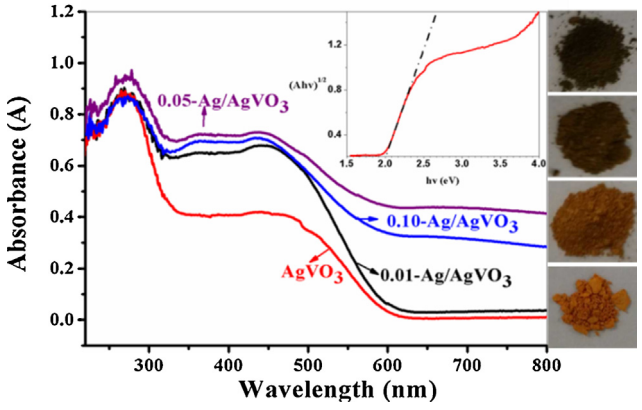

Fig. 6. UV–vis absorption spectra of $AgVO_3$ and $Ag/AgVO_3$ nanoribbons (the insert shows a plot of $(Ah\nu)^{1/2}$ vs energy $h\nu$). (For interpretation of the references to color in text, the reader is referred to the web version of the article.)

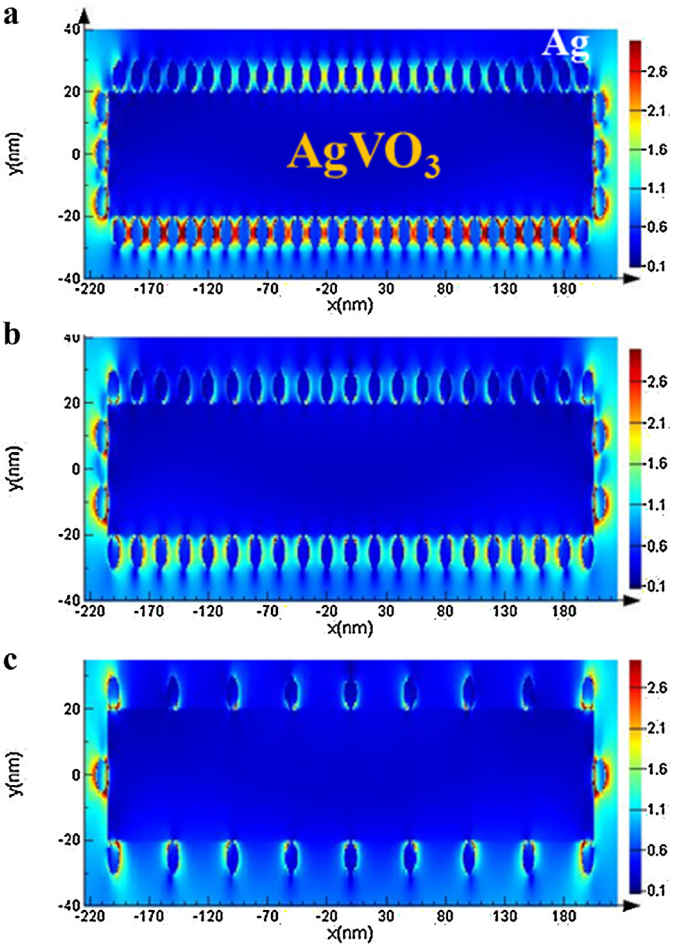

Fig. 8. Electric field distributions calculated at the cross-sections of $Ag/AgVO_3$ nanoribbons using the FDTD method (the thickness and width of simulative $AgVO_3$ nanoribbon are 50 nm and 400 nm, respectively).

(FDTD) method. The amount and size of formed Ag nanoparticles on $AgVO_3$ surfaces varied depending on the amount of added $NaBH_4$. Accordingly, the simulations using varying numbers of Ag nanoparticles on $AgVO_3$ surfaces were performed. Fig. 8 shows the simulated cross-sectional plots of the electric fields of $Ag/AgVO_3$ nanoribbons with increasing number of Ag nanoparticles on the cross sections of $AgVO_3$ nanoribbons (Fig. 8a–c). The local "hot spots" can be seen in regions among nearly touching Ag nanoparticles. This is a well-known phenomenon, corroborated by the

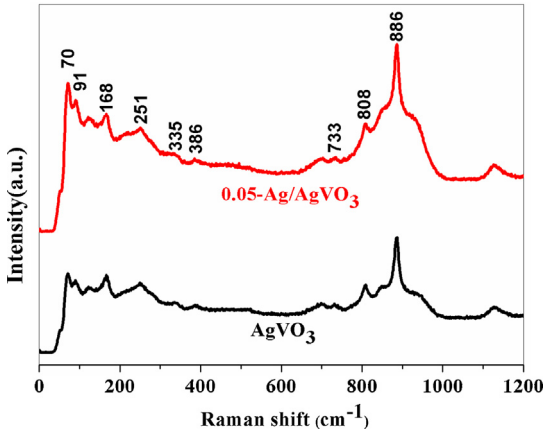

Fig. 7. Raman spectra of the as-prepared $AgVO_3$ and $Ag/AgVO_3$ nanoribbons.

calculations of several research groups [64,65]. Interestingly, we have observed that increasing the numbers of silver nanoparticles on the $AgVO_3$ surface makes the electronic coupling between $AgVO_3$–Ag and Ag–Ag stronger, leading to an electric field enhancement at the gap between the silver nanoparticles. Moreover, the electric field intensity at the $AgVO_3$ surface is stronger than that of the incident electric field. Thus, the photoabsorption (and hence electron–hole pair generation) rate is higher than that of the normal incident light [66,67]. This result suggests that increase appropriately the Ag nanoparticles can facilitate the SPR. However, it does not mean too many silver nanoparticles would have better photocatalytic activity; the excess Ag nanoparticles may cover up the surface of the sample and suppress the absorption of light. The previous results of the UV–vis absorption spectra also confirm the above deduction.

In order to better understand the electronic structures, energy band structures and density of states of the $AgVO_3$ and $Ag/AgVO_3$ plasmonic photocatalysts, the samples were calculated by density functional theory (DFT). Two theoretical structure models were used, corresponding to $AgVO_3$ (Fig. 9a) and $Ag/AgVO_3$ (Fig. 9b) respectively.

The calculations show that $AgVO_3$ has narrow bandgap energy of 2.01 eV, which is in good agreement with the experimental E_g values of 2.0 eV by estimating from the UV–vis absorption spectra. The presence of Ag nanoparticles on $AgVO_3$ surfaces narrowed the band gap energy to 1.50 eV (Fig. 9d) due to the fact that the Ag 5s orbital by association with Ag nanoparticles moves down

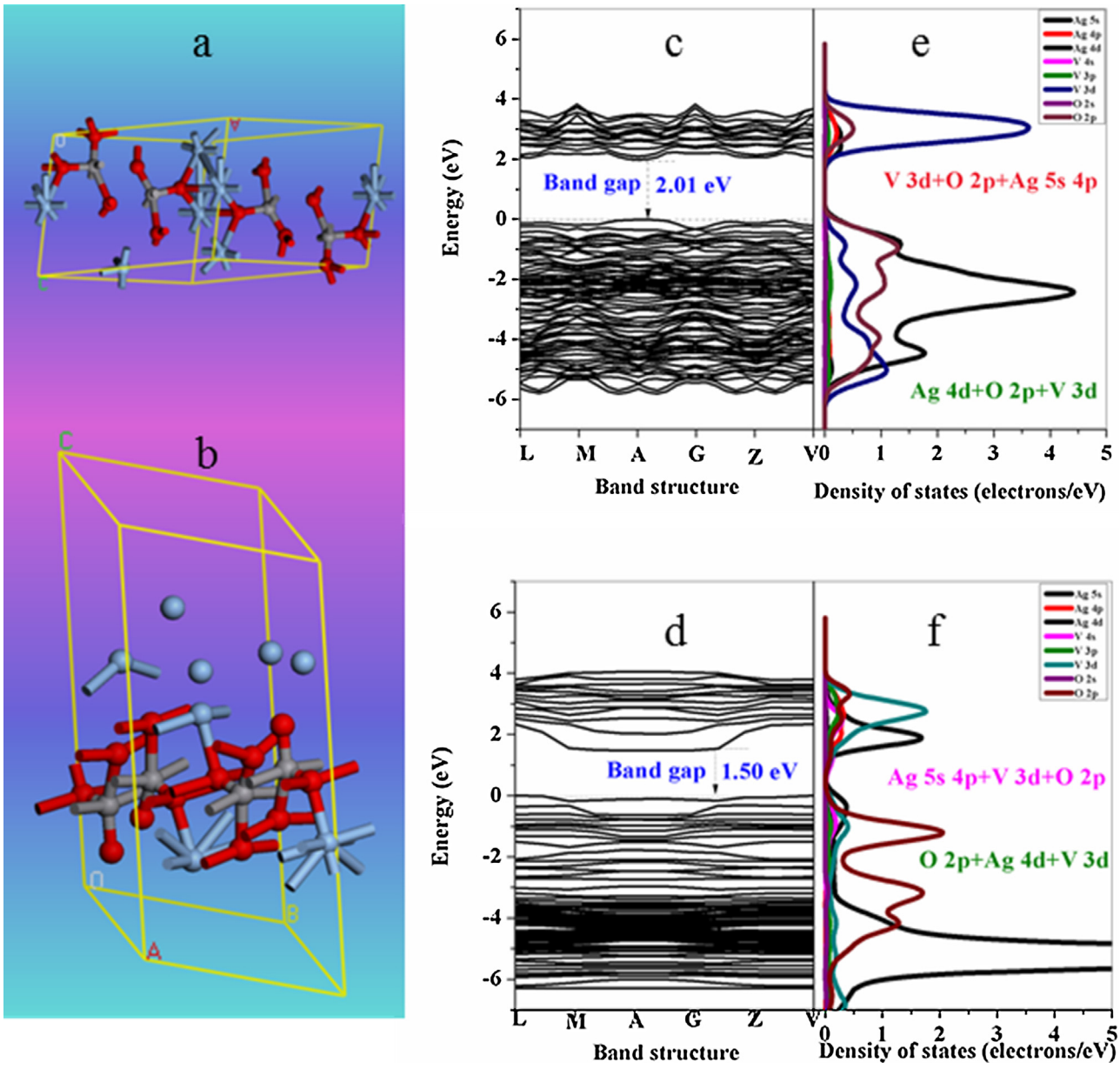

Fig. 9. Crystal structures of $AgVO_3$ (a) and $Ag/AgVO_3$ (b), calculated bandstructures and projected density of states of $AgVO_3$ (c and e) and $Ag/AgVO_3$ (d and f).

the CB after hybridization. Such narrowed band gap energy could enhance the absorption of visible light. The projected density of state analysis indicates that for $AgVO_3$ the conduction band minimum (CBM) is mainly contributed from V 3d orbit, and the valence band maximum (VBM) is mainly composed of Ag 4d and O 2p orbits (Fig. 9e). Moreover, the high hybridization of O atoms with adjacent Ag atoms in the VB meant that the electrons are difficult to be excited. It is due to the fact that large hybrid electron density enhances electrostatic attraction between the nuclei and electrons. For the $Ag/AgVO_3$ (Fig. 9f), Ag 5s orbit dominates the CBM regions, while the VBM is mainly composed of O 2p and Ag 4d orbits. Fortunately, the hybridization of O 2p and Ag 4d orbits of $Ag/AgVO_3$ is much weaker than that of the $AgVO_3$ on the top of the VB, which is beneficial for valence band electrons excite into the conduction band [68]. Taken together, the presence of Ag nanoparticles on $AgVO_3$ surfaces not only causes SPR and enhances the electric field, but also narrow the bandgap energy of $AgVO_3$.

3.4. Photocatalytic activity

The photocatalytic activities of $Ag/AgVO_3$ catalysts were evaluated by comparing degradation rates of basic fuchsin (BF) under visible light irradiation. There was no obvious photocatalytic degradation of BF in the absence of photocatalyst (Fig. 10a). A dark adsorption experiment was also performed to achieve an equilibrium adsorption state, as shown in Fig. S1.

Fig. 10a shows the photodegradation of BF as a function of reaction time. BF was gradually decomposed with reaction time under visible light irradiation. For pure $AgVO_3$, BF decreased 59.1% after 90 min. $Ag/AgVO_3$ manifested remarkably higher photocatalytic activities than that of $AgVO_3$. With increasing the surface Ag content, the photocatalytic activities first increase and then decrease. The presence of 0.01-$Ag/AgVO_3$ resulted in 88.1% of BF decomposed at 90 min. 0.05-$Ag/AgVO_3$ demonstrated the highest efficiency to degrade BF, up to 93.6% at 90 min. It is clear that the Ag nanoparticles on $AgVO_3$ surfaces facilitated the transfer

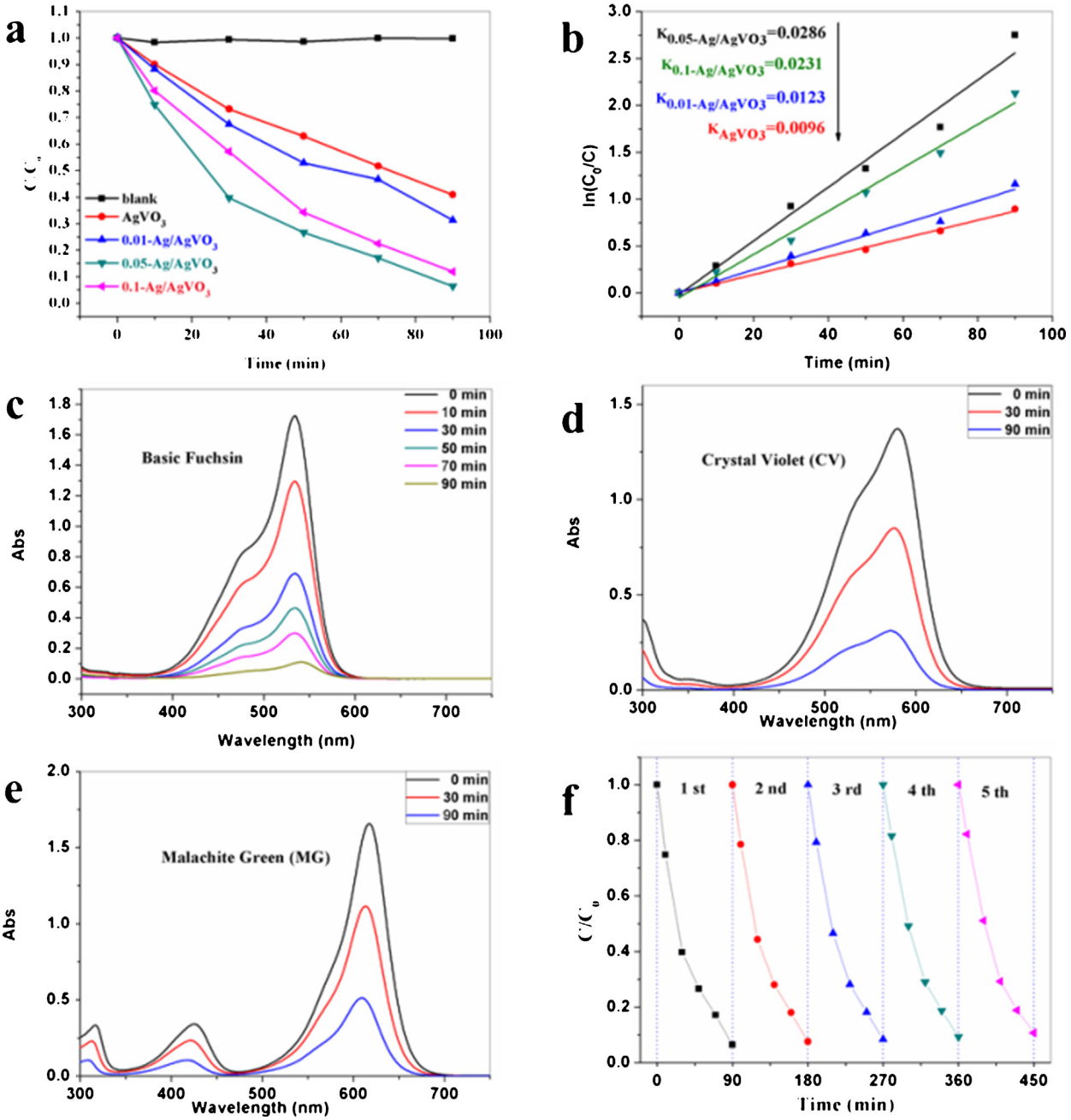

Fig. 10. Photocatalytic activities (a) and pseudo-first-order kinetics (b) of as-prepared photocatalysts for BF degradations; photocatalytic activity of 0.05-Ag/$AgVO_3$ for BF (c), CV (d) and MG (e) degradations; five recycling runs of 0.05-Ag/$AgVO_3$ for BF degradations (f).

of the photogenerated electrons and suppressed the combination of electron–hole pairs. However, the increasing Ag content could cover up the surface of $AgVO_3$, which not only retard the absorption of light but also reduce the surface area available for the reaction on the $AgVO_3$, hence reducing the photocatalytic activity (e.g. 0.10-Ag/$AgVO_3$).

To quantify the degradation rate, the reaction kinetics was described using a pseudo-first-order model $\ln(C/C_0) = k_{app}\ t$ [69], where C and C_0 are BF concentration at time t (min), and $t = 0$; k_{app} (min^{-1}) is the apparent reaction rate constant. The results revealed that 0.05-Ag/$AgVO_3$ plasmonic photocatalyst exhibited the greatest k_{app} value (0.0286 min^{-1}) vs k_{app} value of the pure $AgVO_3$ (i.e. 0.0096 min^{-1}). The changes of UV–vis absorption spectra of BF over the optimum 0.05-Ag/$AgVO_3$ plasmonic photocatalyst are shown in Fig. 10c. BF dye manifested a maximum absorption band at 543 nm. The reaction under visible light irradiation resulted in a transparent solution after 90 min, which is due to the destruction of the chromophoric structures of BF. The other two dyes CV (Fig. 10d) and MG (Fig. 10e) demonstrated similar patterns with 0.05-Ag/$AgVO_3$, but to a less extend. After 90 min irradiation with visible light, 77.5% of CV and 69.1% of MG disappeared from the solution.

The stability and recyclability of the catalysts are important issues in the practice application [70]. The lifetime of catalysts was also evaluated by using 0.05-Ag/$AgVO_3$ plasmonic photocatalyst to react with BF for five times. As shown in Fig. 10f, the photocatalyst demonstrated adequate stability and reusability. Furthermore, the XRD pattern in Fig. S2 shows that there is a negligible change about the phase structure of 0.05-Ag/$AgVO_3$ after repeated photocatalytic reactions, indicating that the sample can work as a stable and efficient visible-light photocatalyst.

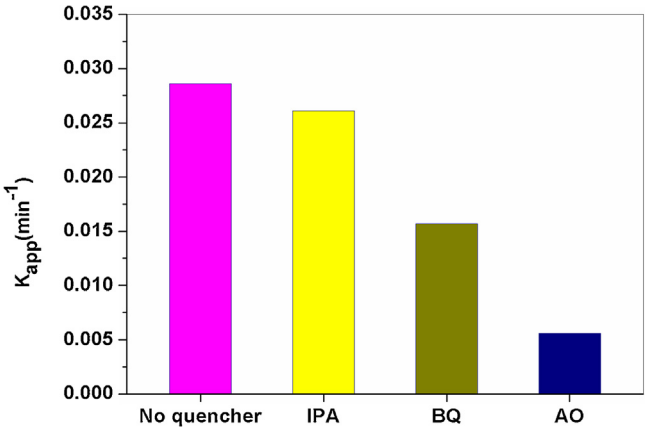

Fig. 11. k_{app} values of 0.05-Ag/$AgVO_3$ plasmonic photocatalyst with selected quenchers.

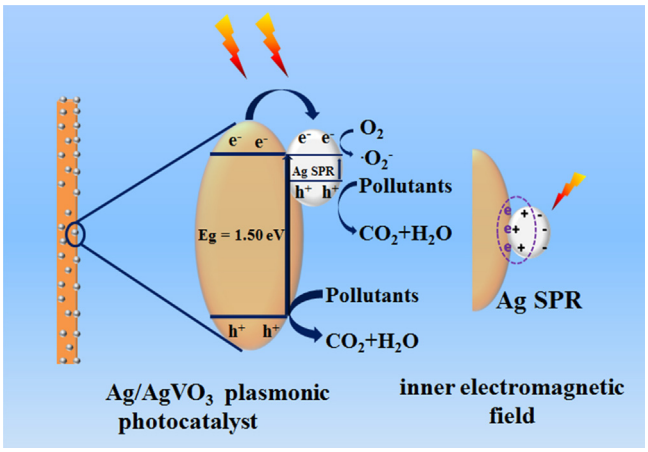

Scheme 2. Proposed mechanism of photocatalytic reaction in Ag/$AgVO_3$ system.

3.5. Photocatalytic reaction mechanism

In general, photocatalytic decompositions of dyes are oxidative processes in which several reactive intermediate species may be involved such as h^+, $^\bullet O_2^-$ and $^\bullet OH$ [71–73]. In this study, several different scavengers ammonium oxalate (AO), benzoquinone (BQ) and isopropanol (IPA) were selected to quench h^+, $^\bullet O_2^-$ and $^\bullet OH$ if formed during the degradation of BF. It was apparent that all these scavengers could partially suppress the reaction resulting in diminishing k_{app} values compared to that in the absence of scavengers (Fig. 11). The k_{app} decreased in the order of $k_{app,\,AO} < k_{app,\,BQ} < k_{app,\,IPO}$, indicating that h^+ and $^\bullet O_2^-$ are the main oxidative species in the reactions. $^\bullet O_2^-$ is commonly formed through the direct interactions of photogenerated electrons with the surface adsorbed oxygen on the photocatalyst [74].

Furthermore, the photocatalytic property of the photocatalyst is associated with its band structure. The band edge positions of both the conduction and the valence bands can be determined using a simple approach [75]. The conduction band edge (E^0_{CB}) of a semiconductor at the point of zero charge (pH_{ZPC}) can be predicted using the following equation: $E^0_{CB} = X - E^e - 0.5E_g$. Where X is the absolute electronegativity of the semiconductor, E^e is the energy of free electrons on the hydrogen scale (4.5 eV), and E_g is the band gap of the semiconductor. The DFT calculation results showed the band gap energy of Ag/$AgVO_3$ was ~1.5 eV (Fig. 9d). The X value for $AgVO_3$ was 5.86 eV. Consequently, the E_{CB} value of $AgVO_3$ was calculated to be 0.61 eV, and the E_{VB} value was estimated to be 2.11 eV.

Based on the experimental results, the proposed photocatalytic reaction mechanism is illustrated in Scheme 2. When Ag/$AgVO_3$ was subjected to the visible light irradiation, both $AgVO_3$ and Ag nanoparticles were excited with photogenerated electrons and holes produced. The produced electrons in the conduction band of $AgVO_3$ would transfer quickly to Ag nanoparticles because of the high conductivity and electron-storing capacity of the silver nanoparticles [76]. This could help the reduction of the recombination probability of formed elections and holes. Moreover, the excess electrons would move away from the $AgVO_3$, which diminishes the reduction of Ag^+, leading to more stable Ag/$AgVO_3$ photocatalyst. The more and stable photogenerated holes could oxidize the dye molecules directly on $AgVO_3$ surfaces, which is consistent with the fact that AO demonstrated as the most efficient scavenger to inhibit the oxidative reaction by consuming the formed holes. The photogenerated electrons in Ag nanoparticles and those transferred from $AgVO_3$ could be trapped by O_2 to form $^\bullet O_2^-$ reactive oxygen species [77]. The SPR effect which is produced by the collective oscillations of metal Ag surface electrons could induce enhancement of the local inner electromagnetic field [78] as evidenced in the FDTD simulations (Fig. 8). The electrons and holes generated in $AgVO_3$ could also be separated efficiently with the help of the local electromagnetic field. The similar results have been reported on Ag_3PO_4 and Ag_2O [79] photocatalysts. Those effects could stabilize the structures of Ag-based materials.

Compared with the standard reduction potential of $^\bullet OH/H_2O$ (2.27 eV) or $^\bullet OH/OH^-$ (2.38 eV), the VBM potential of h^+ on $AgVO_3$ surfaces (2.11 eV) is not high enough to oxidize H_2O or OH− into $^\bullet OH$ [80]. Thus, the photocatalytic degradation of BF could be primarily attributed to reacting with h^+ instead of $^\bullet OH$ radicals. Furthermore, the CB electrons of $AgVO_3$ (0.61 eV) show a poor reduction power and are not enough to reduce O_2 to $^\bullet O_2^-$ radicals because the reduction potential of $O_2/^\bullet O_2^-$ is −0.33 eV [81]. The electrons transferred from $AgVO_3$ and the plasmon-excited electrons of Ag are assumed in the Ag nanoparticles surface to reduce O_2 to $^\bullet O_2^-$, which further reacts with BF. The presence of BQ diminished the degradation efficiency of BF due to the consumption of $^\bullet O_2^-$ radicals by BQ.

4. Conclusions

In summary, the novel one-dimension Ag/$AgVO_3$ plasmonic photocatalysts were synthesized via in-suit reduction reaction of $AgVO_3$ by $NaBH_4$ at room temperature. Synthesized Ag/$AgVO_3$ demonstrated enhanced visible light-catalyzed reaction efficiencies for BF, CV and MG dyes compared to $AgVO_3$. The enhanced photocatalytic performance was attributed to the great conductivity and electron-storing capacity of Ag nanoparticles, which facilitate the charge transfer between $AgVO_3$ and Ag nanoparticles. The finite difference time domain (FDTD) simulation analysis indicates the formed Ag nanoparticles induce the localized surface plasmon resonance (SPR) leading to increased electric field and the enhanced absorption of visible light. In addition, the presence of Ag nanoparticles could narrow the bandgap energy from 2.01 for $AgVO_3$ to 1.50 for Ag/$AgVO_3$. The hybridization of O 2p and Ag 4d orbits of $AgVO_3$ is weak, which facilitates transfer of valence band electrons into the conduction band. The present study will benefit the development of the other novel Ag-based plasmonic photocatalysts to meet the environmental demands in the future.

Acknowledgements

The authors greatly acknowledge the National Natural Science Foundation of China (Nos. 21177055 and 51278242), the Natural Science Foundation of Jiangsu Province (BK2012732), the Jiangsu Provincial Science and Technology Supporting Program

(No. BE2012116), the Jiangsu Province Graduate Student Scientific Research Innovation Project (KYLX0050), and the China Postdoctoral Science Foundation funded the 54th batches surface (2013M541646).

The authors thank Dr. Li H. (Department of Plant, Soil and Microbial Sciences, Michigan State University) for his great help at language modification and composition suggestion, and Dr. Shi X B. (Institute of Functional Nano & Soft Materials (FUNSOM) and Collaborative Innovation Center of Suzhou Nano Science and Technology, Soochow University), Dr. Yuan L (State Key Laboratory of Inorganic Synthesis and Preparative Chemistry, College of Chemistry, Jilin University) and Dr. Wu H W (National Laboratory of Solid State Microstructures & Department of Physics, Nanjing University)for their helps in discussing the experimental results.

The authors also acknowledge the suggestions made by the reviewer which have helped to improve the quality of the paper considerably.

Appendix A. Supplementary data

Supplementary data associated with this article can be found, in the online version, at http://dx.doi.org/10.1016/j.apcatb.2014.08.015.

References

[1] M.A. Shannon, P.W. Bohn, M. Elimelech, J.G. Georgiadis, B.J. Marinas, A.M. Mayes, Nature 452 (2008) 301–310.
[2] L.H. Yu, Y. Huang, G.G. Xiao, D.Z. Li, J. Mater. Chem. A 1 (2013) 9637–9640.
[3] G. Liu, Y.N. Zhao, C.H. Sun, F. Li, G.Q. Lu, H.M. Cheng, Angew. Chem. Int. Ed. 120 (2008) 4592–4596.
[4] H.X. Chang, H.K. Wu, Energy Environ. Sci. 6 (2013) 3483–3507.
[5] M. Zhang, C.C. Chen, W.H. Ma, J.C. Zhao, Angew. Chem. Int. Ed. 47 (2008) 9730–9733.
[6] J.B. Joo, M. Dahl, N. Li, F. Zaera, Y.D. Yin, Energy Environ. Sci. (2013) 2082–2092.
[7] B. Pan, Q.H. Xie, H.M. Wang, J. Zhu, Y.F. Zhang, W.Y. Su, X.X. Wang, J. Mater. Chem. A 1 (2013) 6629–6634.
[8] R. Asahi, T. Morikawa, T. Ohwaki, K. Aoki, Y. Taga, Science 293 (2001) 269–271.
[9] P.D. Tran, L.H. Wong, J. Barber, J.S.C. Loo, Energy Environ. Sci. 5 (2012) 5902–5918.
[10] K.S. Yang, Y. Dai, B.B. Huang, J. Phys. Chem. C 111 (2007) 18985–18994.
[11] X.B. Chen, B. Clemens, J. Am. Chem. Soc. 130 (2008) 5018–5019.
[12] J.K. Zhou, Y.X. Zhang, X.S. Zhao, A.K. Ray, Ind. Eng. Chem. Res. 45 (2006) 3503–3511.
[13] B. Peng, X.W. Meng, F.Q. Tang, X.L. Ren, D. Chen, J. Ren, J. Phys. Chem. C 113 (2009) 20240–20245.
[14] Z.G. Zou, J.H. Ye, K. Sayama, H. Arakawa, Nature 414 (2001) 625–627.
[15] D. Chen, H. Zhang, Y. Liu, J.H. Li, Energy Environ. Sci. 6 (2013) 1362–1387.
[16] W. Zhao, Y.F. Liu, J.J. Liu, P. Chen, I.W. Chen, F.Q. Huang, J.H. Lin, J. Mater. Chem. A 1 (2013) 7942–7948.
[17] Z.J. Chen, S.K. Gao, R.H. Li, M.D. Wei, K.M. Wei, H.S. Zhou, Electrochim. Acta 53 (2008) 8134–8137.
[18] L.Q. Mai, L. Xu, Q. Gao, C.H. Han, B. Hu, Y.Q. Pi, Nano Lett. 10 (2010) 2604–2608.
[19] H. Xu, H.M. Li, L. Xu, C.D. Wu, G.S. Sun, Y.G. Xu, J.Y. Chu, Ind. Eng. Chem. Res. 48 (2009) 10771–10778.
[20] L.C. Chen, G.T. Pan, T.C.K. Yang, T.W. Chung, C.M. Huang, J. Hazard. Mater. 178 (2010) 644–651.
[21] J. Ren, W.Z. Wang, M. Shang, S.M. Sun, L. Zhang, J. Chang, J. Hazard. Mater. 183 (2010) 950–953.
[22] H.F. Shi, Z.S. Li, J.H. Kou, J.H. Ye, Z.G. Zou, J. Phys. Chem. C 115 (2011) 145–151.
[23] W.G. Wang, B. Cheng, J.G. Yu, G. Liu, W.H. Fan, Chem. Asian J. 7 (2012) 1902–1908.
[24] S.Y. Zhang, W.Y. Li, C.S. Li, J. Chen, J. Phys. Chem. B 110 (2006) 24855–24863.
[25] S.J. Bao, Q.L. Bao, C.M. Li, T.P. Chen, C.Q. Sun, Z.L. Dong, Y. Gan, J. Zhang, Small 3 (2007) 1174–1177.
[26] J.M. Song, Y.Z. Lin, H.B. Yao, F.J. Fan, X.G. Li, S.H. Yu, ACS Nano 3 (2009) 653–660.
[27] M.S. Zhu, P.L. Chen, M.H. Liu, J. Mater. Chem. 22 (2012) 21487–21494.
[28] Y.P. Bi, S.X. Ouyang, J.Y. Cao, J.H. Ye, Phys. Chem. Chem. Phys. 13 (2011) 10071–10075.
[29] Y.J. Wang, R. Shi, J. Lin, Y.F. Zhu, Energy Environ. Sci. 4 (2011) 2922–2929.
[30] Q. Gu, J.L. Long, L.Z. Fan, L.M. Chen, L.L. Zhao, H.X. Lin, X.X. Wang, J. Catal. 303 (2013) 141–155.
[31] Z.J. Chen, Z.H. Guan, M.R. Li, Q.H. Yang, C. Li, Angew. Chem. Int. Ed. 50 (2011) 4913–4917.
[32] N. Sobana, M. Muruganadham, M. Swaminathan, J. Mol. Catal. A 258 (2006) 124–132.
[33] J. Ren, W.Z. Wang, S.M. Sun, L. Zhang, J. Chang, Appl. Catal., B 92 (2009) 50–55.
[34] M. Murdoch, G.I.N. Waterhouse, M.A. Nadeem, J.B. Metson, M.A. Keane, R.F. Howe, J. Llorca, H. Idriss, Nat. Chem. 3 (2011) 489–492.
[35] W.B. Wang, F.F. Wang, Y.R. Kang, A.Q. Wang, RSC Adv. 3 (2013) 11515–11520.
[36] Y.C. Liang, C.C. Wang, C.C. Kei, Y.C. Hsueh, W.H. Cho, T.P. Perng, J. Phys. Chem. C 115 (2011) 9498–9502.
[37] B. Zhou, X. Zhao, H.J. Liu, J.H. Qu, C.P. Huang, Sep. Purif. Technol. 77 (2011) 275–282.
[38] D.J. Wang, G.L. Xue, Y.Z. Zhen, F. Fu, D.S. Li, J. Mater. Chem. 22 (2012) 4751–4758.
[39] N.K. Allam, C.W. Yen, R.D. Near, M.A. El-Sayed, Energy Environ. Sci. 4 (2011) 2909–2914.
[40] H.J. Chen, L. Shao, Q. Li, J.F. Wang, Chem. Soc. Rev. 42 (2013) 2679–2724.
[41] K. Kalyanasundaram, Photochemistry 41 (2013) 182–265.
[42] X.M. Zhou, G. Liu, J.G. Yu, W.H. Fan, J. Mater. Chem. 22 (2012) 21337–21354.
[43] J. Sía, G. Tagliabue, P. Friedli, J. Szlachetko, M.H. Rittmann-Frank, F.G. Santomauro, C.J. Milne, H. Sigg, Energy Environ. Sci. 6 (2013) 3584–3588.
[44] A. Bumajdad, M. Madkour, Phys. Chem. Chem. Phys. 16 (2014) 7146–7158.
[45] P. Wang, B.B. Huang, Q. Zhang, X. Zhang, X. Qin, Y. Dai, J. Zhan, J. Yu, H. Liu, Z. Lou, Chem. Eur. J. 16 (2010) 10042–10047.
[46] P. Wang, B.B. Huang, Z.Z. Lou, X.Y. Zhang, X.Y. Qin, Y. Dai, Z.K. Zheng, X.N. Wang, Chem. Eur. J. 16 (2010) 538–544.
[47] P. Wang, B.B. Huang, X.Y. Qin, X.Y. Zhang, Y. Dai, J.Y. Wei, M.H. Whangbo, Angew. Chem. Int. Ed. 41 (2008) 7931–7933.
[48] Y.G. Lin, Y.K. Hsu, Y.C. Chen, S.B. Wang, J.T. Miller, L.C. Chen, K.H. Chen, Energy Environ. Sci. 5 (2012) 8917–8922.
[49] Z.X. Ji, M.N. Ismail, D.M. Callahan Jr., E. Pandowo, Z.H. Cai, T.L. Goodrich, K.S. Ziemer, J. Warzywoda, A. Sacco Jr., Appl. Catal., B 102 (2011) 323–333.
[50] M.S. Zhu, P.L. Chen, M.H. Liu, ACS Nano 5 (2011) 4529–4536.
[51] M.S. Zhu, P.L. Chen, M.H. Liu, Langmuir 28 (2012) 3385–3390.
[52] M.D. Segall, P.J.D. Lindan, M.J. Probert, C.J. Pickard, P.J. Hasnip, S.J. Clark, M.C. Payne, J. Phys.: Condens. Matter 14 (2002) 2717–2744.
[53] G.T. Li, K.H. Wong, X.W. Zhang, C. Hu, J.C. Yu, R.C.Y. Chan, P.K. Wong, Chemosphere 76 (2009) 1185–1191.
[54] N. Zhang, S.Q. Liu, X.Z. Fu, Y.J. Xu, J. Phys. Chem. C 115 (2011) 9136–9145.
[55] M.R. Parida, C. Vijayan, C.S. Rout, C.S.S. Sandeep, R. Philip, Appl. Phys. Lett. 100 (2012) 121119.
[56] Q. Zhu, W.S. Wang, L. Lin, G.Q. Gao, H.L. Guo, H. Du, A.W. Xu, J. Phys. Chem. C 117 (2013) 5894–5900.
[57] S.Q. Liang, J. Zhou, X.L. Zhang, Y. Tang, G.Z. Fang, T. Chen, X.P. Tan, CrystEngComm 15 (2013) 9869–9873.
[58] M.W. Shao, L. Lu, H. Wang, S. Wang, M.L. Zhang, D.D.D. Ma, S.T. Lee, Chem. Commun. 23 (2008) 2310–2312.
[59] W. Teng, X.Y. Li, Q.D. Zhao, J.J. Zhao, D.K. Zhang, Appl. Catal., B 125 (2012) 538–545.
[60] P. Ju, H. Fan, B.L. Zhang, K. Shang, T. Liu, S.Y. Ai, D. Zhang, Sep. Purif. Technol. 109 (2013) 107–110.
[61] L. Tong, Z. Li, T. Zhu, H. Xu, Z. Liu, J. Phys. Chem. C 112 (2008) 7119–7123.
[62] Y. Kim, H. Na, Y.W. Lee, H. Jang, S.W. Han, D. Min, Chem. Commun. 46 (2010) 3185–3187.
[63] H. Zhang, X.F. Fan, X. Quan, S. Chen, H.T. Yu, Environ. Sci. Technol. 45 (2011) 5731–5736.
[64] F. Le, D.W. Brandl, Y.A. Urzhumov, H. Wang, J. Kundu, N.J. Halas, J. Aizpurua, P. Nordlander, ACS Nano 2 (2008) 707–718.
[65] W.B. Hou, Z.W. Liu, P. Pavaskar, W.H. Hung, S.B. Cronin, J. Catal. 277 (2011) 149–153.
[66] H. Choi, S.J. Ko, Y. Choi, P. Joo, T. Kim, B.R. Lee, J.W. Jung, H.J. Choi, M. Cha, J.R. Jeong, I.W. Hwang, M.H. Song, B.S. Kim, J.Y. Kim, Nat. Photonics 7 (2013) 732–738.
[67] Z.W. Liu, W.B. Hou, P. Pavaskar, M. Aykol, S.B. Cronin, Nano Lett. 11 (2011) 1111–1116.
[68] S.M. Wang, D.L. Li, C. Sun, S.G. Yang, Y. Guan, H. He, Appl. Catal., B 144 (2014) 885–892.
[69] Y. Li, X. Li, J. Li, J. Yin, Water Res. 40 (2006) 1119–1126.
[70] J.F. Ma, J. Zou, L.Y. Li, C. Yao, Y. Kong, B.Y. Cui, R.L. Zhu, D.L. Li, Appl. Catal., B 144 (2004) 36–40.
[71] X.F. Zhou, C. Hu, X.X. Hu, T.W. Peng, J.H. Qu, J. Phys. Chem. C 114 (2010) 2746–2750.
[72] Y.Q. Yang, G.K. Zhang, S.J. Yu, X. Sheng, Chem. Eng. J. 162 (2010) 171–177.
[73] Y.Y. Li, J.S. Wang, H.C. Yao, L.Y. Dang, Z.J. Li, J. Mol. Catal. A: Chem. 334 (2011) 116–122.
[74] J.G. Yu, G.P. Dai, B.B. Huang, J. Phys. Chem. C 113 (2009) 16394–16401.
[75] H. Xu, H. Li, C. Wu, J. Chu, Y. Yan, H. Shu, Z. Gu, J. Hazard. Mater. 153 (2008) 877–884.
[76] Y.P. Liu, L. Fang, H.D. Lu, L.J. Liu, H. Wang, C.Z. Hu, Catal. Commun. 17 (2012) 200–204.
[77] J.G. Yu, J.F. Xiong, B. Cheng, S.W. Liu, Appl. Catal., B 60 (2005) 211–221.
[78] Y.P. Liu, L. Fang, H.D. Lu, Y.W. Li, C.Z. Hua, H.G. Yu, Appl. Catal., B 115–116 (2012) 245–252.
[79] X. Wang, S. Li, H. Yu, J. Yu, S. Liu, Chem. Eur. J. 17 (2011) 7777–7780.
[80] H.F. Cheng, B.B. Huang, Y. Dai, X.Y. Qin, X.Y. Zhang, Langmuir 26 (2010) 6618–6624.
[81] J. Kim, C.W. Lee, W. Choi, Environ. Sci. Technol. 44 (2010) 6849–6854.